

*Modeling for Direct Drive Fusion Implosions:
Cryogenic Target Filling at Arbitrary Viewing
Angles and Yield Prediction*

Simon Narang

Sutherland High School

Pittsford, New York

November 2019

Advisors: M. D. Wittman, D. Bredezen

Laboratory for Laser Energetics

University of Rochester

Rochester, New York

Abstract

Cryogenic targets for nuclear fusion are cooled to produce solid deuterium-tritium (DT) layers on their interiors. A new system, the fill tube, is being developed to improve cryogenic target quality and thus plasma compression. Due to physical constraints on the OMEGA target chamber, the fill tube can only be fielded on the laser at an angle not perpendicular to gravity. In this work, a new model, *SPARROW*, was developed to predict the final layer thickness of uncooled DT-liquid-filled targets viewed from arbitrary angles. In previous work, x-ray micrographs of liquid-filled targets were studied to obtain equations relating the size of the bubble above the liquid meniscus to the target's volume of fuel; this volume correlates with final DT layer thickness. With these equations, this work's newly developed model can automate cryogenic filling to a desired thickness within $\pm 2\text{-}\mu\text{m}$ accuracy. This will enable the final thickness to be determined prior to solidification. Further, a machine learning model was created to quantify the increase in neutron yield that can be attained if cryogenic target quality is improved. Nineteen models were trained on OMEGA data. The models were then compared for accuracy. Testing of the most accurate model revealed that target quality has a 17% impact on yield.

1 Introduction

Nuclear inertial confinement fusion (ICF) occurs between hydrogen atoms when the strong nuclear forces concentrated in nuclei overcome the repulsive electrostatic forces of protons. When enough atoms fuse, energetic neutrons are released that can be used for energy production. At the Laboratory for Laser Energetics (LLE), fusion is achieved with the sixty beam, 30 kJ OMEGA laser. LLE conducts ICF experiments with the OMEGA laser by concentrating energy on a target of $\sim 860 \mu\text{m}$ diameter to uniformly compress the fuel inside. Targets are filled with a composite fuel of deuterium and tritium (DT) due to the high nuclear cross-section of the fuel.¹

Two indicators of progress toward ignition are the neutron yield (Y), the number of neutrons emitted by the fused DT in a target, and the areal density (ρR), a figure of merit as to how much fuel has been compressed. Target and layer imperfections are known to decrease Y and ρR .

Condensable hydrocarbons are created by the radioactive and high pressure environment in which targets are currently permeated with DT fuel. The tritium that dissolves through the target wall during permeation results in β -electron damage, breaking bonds in the polymer target and releasing short-chain hydrocarbons. These condense on the target when it is cooled to liquid and solid hydrogen temperatures. These target imperfections impact Y and ρR .² A new “fill-tube” system seeks to increase Y and ρR by reducing these imperfections such that targets are uniform enough to be pressurized to 100 Gbar. The fill-tube system also decreases particulate contamination. Targets are currently transferred to multiple locations before implosion. The fill tube will fill targets directly on OMEGA, eliminating points of contamination. Liquid DT enters the target through the fill tube and forms a liquid meniscus that is imaged by an x-ray camera. When the target is frozen, the DT forms into a uniform solid layer. This work seeks to predict the thickness of that solid layer based on x-ray images of the meniscus taken at any angle. A model was built for this purpose and tested on targets imaged in the horizontal view. These tests show the model’s predictions to be within the $2 \mu\text{m}$ accuracy specification of LLE’s experimental program.

This work also seeks to quantify the improvement to Y that these target and layer quality

improvements will provide using a machine learning model. Nineteen machine learning models were compared for accuracy against each other as well as two “control” models. The most accurate model showed an accuracy improvement of 17% over previous models.

The outline of this report is as follows. Section 2 describes the importance of cryogenic targets to nuclear fusion, how they are formed, how they are characterized, and the purpose of the new cryogenic fill-tube system. Section 3 describes how this work’s first code, *SPARROW*, was developed and tested to enable the formation of cryogenic targets on the fill tube. Section 4 describes how this work’s machine learning model was developed and tested to quantify the significance of the fill-tube to nuclear fusion.

2 Cryogenic Target Formation

2.1 Layering

Cryogenic targets contain frozen DT. As compared to targets filled with gaseous DT, cryogenic targets enable a higher density of fuel to be contained in the target³ which increases Y and ρR . The current method for fielding cryogenic targets on OMEGA involves filling targets over 18 hours; during this period, DT is gradually compressed to high pressure (up to 1000 atm). A pressure gradient across the shell wall causes DT to diffuse through the target’s polymer shell and fill the interior.

After permeation, the temperature is lowered to ~ 20 K. This reduces the permeability of the target walls; hence, the gaseous fuel cannot escape. Next, the target is transferred to a “layering sphere” where its temperature is decreased (“ramped down”) further over several hours until the fuel solidifies into a spherical layer, starting as a single crystal and becoming uniform in a process known as β -layering.⁴ In β -layering, radioactive tritium in the DT emits high-energy β particles that locally heat the region where they are produced. Thus, thicker regions heat more than thinner regions. The result is a uniform solid layer on the interior of the target.⁵ This layer is quantified by how radially thick it is. At present, it is yet to be determined what layer thickness is ideal for plasma compression.

2.2 Characterization

While targets are layered, a charged-coupled device (CCD) camera takes optical shadowgraphy images. The CCD camera captures images formed by light rays reflected by the inner surface of the solid DT layer. These images show a narrow bright ring that is currently used on OMEGA to measure target layer thickness and uniformity.⁶

The CCD also measures various target parameters (e.g., the initial location of the DT crystal). The initial location of the crystal is described by the observed horizontal and vertical offset of the crystal from the target center. This measurement is used in the machine learning model in Section 4.

X-ray cameras are not currently in use for target characterization on the OMEGA laser. However, they will be used on the new fill-tube system. X-ray images were used to develop this work’s filling model. Images are formed by x rays that are emitted from a 60-kVp, 4- μm spot size point source and pass through the target and into the camera, as shown in Figure 2.1. X rays 1 and 2 are deflected because they are nearly tangential to interfaces. Due to this deflection, these x rays are not detected by the camera where they would be if they traveled in a straight line from the point source. Dark regions are thus formed. These dark regions form shapes (circles and ellipses).

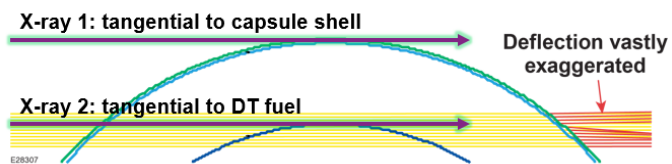


Figure 2.1: Rays tangential to (1) the target and (2) the inner surface of the solid DT. Although they are shown nearly parallel, they both originate from the same x-ray point source. After propagating through the target, they hit the camera. Rays are refracted close to the interfaces. As a result, the camera sees two dark circles (in the case of a uniform solid layer).

The dark areas in the images of Figure 2.2 indicate interfaces between different media. The “bubble” in liquid fuel shows a dark circle (the target shell), and the contained region of gas (the interface between gas and liquid DT). A good approximation of this meniscus bubble can be represented as an ellipse. The final fuel layer shows the same target shell and a concentric circle (the interface between gas and solid DT).

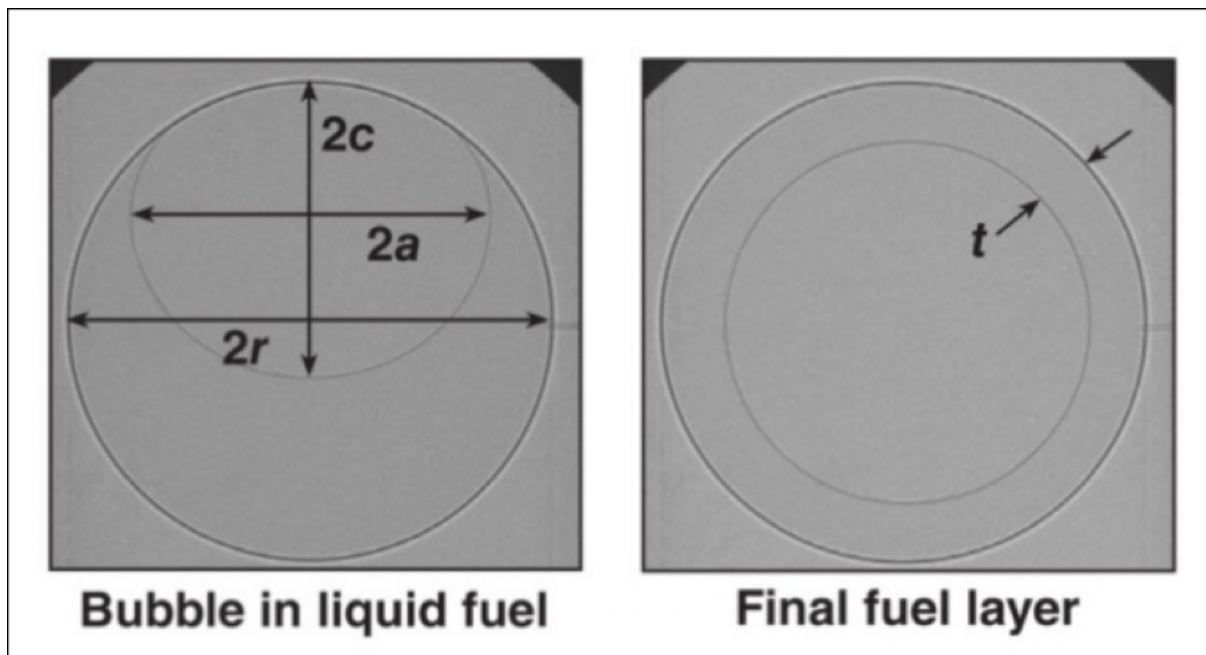


Figure 2.2: X-ray images of a liquid-filled target before and after freezing.⁷

2.3 New Cryogenic Fill-Tube System for OMEGA

The cryogenic fill-tube system is shown schematically in Figure 2.3. The target is filled with liquid DT from the tritium glovebox through the fill tube. The fill-tube heater is used to control the temperature at the interface between the layering sphere and the fill tube. When the interface drops below the freezing point, a solid freeze-plug forms. This stops liquid DT from moving into or out of the target. The target then begins to freeze. The target is viewed with an x-ray camera and an optical shadowgraphy camera.

The new fill-tube filling process was previously automated using a proportional-integral-derivative (PID) control loop that leverages the x-ray camera to adjust the temperature according to the difference between the amount of fuel currently contained in the target and the amount of fuel desired, such that the desired amount enters.⁷

The cryogenic fill-tube fixture to be fielded on OMEGA is shown in Figure 2.4a, and a mounted prototype is shown in Figure 2.4b, viewed perpendicular to gravity. A viewing angle perpendicular to gravity is not geometrically possible. Laser entrances, indicated by blue cylinders, block the x-ray camera from lying horizontally. Thus, $\theta = 23.97^\circ$ below

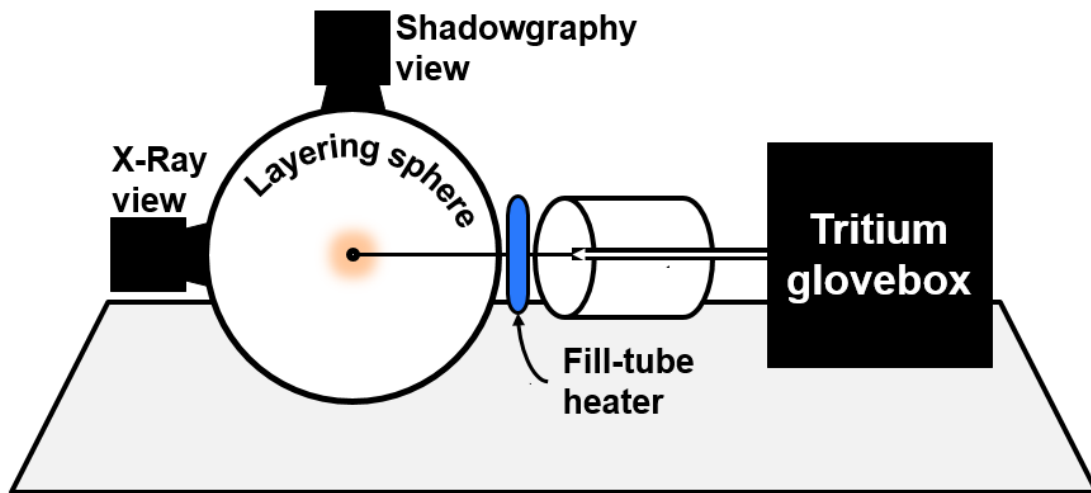


Figure 2.3: Cryogenic fill-tube schematic. The target is filled with DT through a $10\text{-}\mu\text{m}$ -diameter tube; DT is formed in the tritium glovebox shown on the right.

horizontal (position 3) was selected as the optimal choice of the options available because it is closest to horizontal. However, there is currently no experimental setup to image targets at angles other than the horizontal. Ergo, it remains unknown if a greater viewing angle impacts the accuracy of a fill level.

When the vertical angle θ is different from 0, the image of the elliptical meniscus changes location and eccentricity. The reason for this is that x rays passing through the liquid project different cross-sections of the meniscus bubble on the camera depending on the angle. This is addressed in the following section.

3 Layer Thickness Control Model

3.1 Ray-Tracing Simulation

The target-filling automation software must function with x-ray images taken at any angle to the horizontal because in the future the cryogenic fill-tube mechanism may be mounted at angles other than 23.97° . This work addresses this task by modifying a *Matlab* code to simulate the images of targets at all angles. This simulation was run at an array of distinct thicknesses and viewing angles in order to create a model for the predetermination of layer

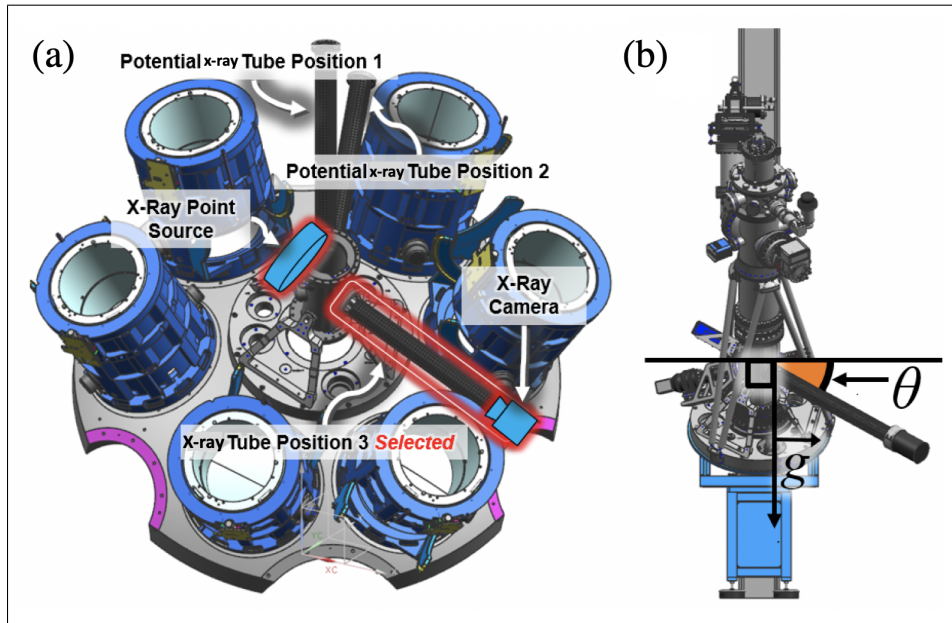


Figure 2.4: Cryogenic fill-tube fixture to be fielded on port H5 of OMEGA. The x-ray camera is located at the end of a black carbon fiber tube. The three black tubes in (a) represent potential x-ray tube mounting positions. The selected tube position will angle down at $\theta = 23.97^\circ$.

thickness as a function of viewing angle and the size of the gaseous bubble in an unfrozen target.

In previous work, final thickness data from deuterium-filled targets had been used to establish the relationship between three measurements of the meniscus bubble and the final layer thickness. Note that these relationships *only* apply to OMEGA targets ($r = 430 \mu\text{m}$ in Figure 2.2). The vertical offset Δy between the centers of the meniscus ellipse and target circle as a function of thickness T is

$$\Delta y(T) = 1.17T + 21.72 \quad (1)$$

where Δy and T are in μm . The semi-major axis of the ellipse a as a function of T is

$$a(T) = -1.27T + 437.14 \quad (2)$$

where a is in μm . The semi-minor axis of the ellipse c as a function of T is

$$c(T) = -1.27T + 432.79 \quad (3)$$

where c is in μm . Note that these equations were developed using only OMEGA targets

over the range $19.6 \leq t \leq 115.8 \mu\text{m}$. This work used Equations (1), (2) and (3) to develop a thickness predetermination ray-tracing code, *SPARROW*. For a given thickness T , *SPARROW* forms an elliptical meniscus given by Equations (1), (2) and (3).

To predetermine thickness, *SPARROW* simulates the x-ray images of targets taken at arbitrary angles for a number of thicknesses T . It simulates the target sphere and x-ray point source as objects in 3D space (see Figure 3.1). Then, the "orthogonal plane" is drawn. This goes through the target center and is orthogonal to the line of sight between the x-ray camera and point source. When *SPARROW* is run, the intersection circle between the target and this orthogonal plane is calculated. Iterating around this circle, the code calculates the locus of points where x rays are tangential to the outer target shell (depicted in Figure 2.1).

The points are calculated by minimizing the dot product between the x rays from the source and lines drawn normal to the target surface using the *fmincon* function in Matlab. While the tangent points to the outer circle can be calculated from Figure 3.1 using elementary trigonometry, *fmincon* was used to test the algorithm. The dot-product-minimization routine is subsequently re-executed on the ellipsoidal region of space above the liquid fuel, defined by Equations (1), (2) and (3). The simulation does not factor in the small deflection experienced by the rays passing through the target. However, it meets the accuracy specification of LLE's experimental program regardless.

fmincon is required because the meniscus bubble is vertically offset from the center of the target (about which the x-ray camera is angled). It is also not spherically symmetric. Therefore, each x ray needs to be traced to calculate a locus of points to form the simulated image. *fmincon* locates the point of tangency between each ray and the bubble.

For certain random x rays, *fmincon* fails to calculate their point of tangency to the target. It thus outputs a point of tangency very far away from the target. *SPARROW* removes these by discarding tangency points whose perpendicular distance to the orthogonal plane is greater than $50 \mu\text{m}$. After outlier point removal, the two loci represent the x-ray image of a target for a specified thickness, viewing angle and target diameter.

Cryogenic targets on OMEGA have been shot with solid layer thicknesses between 40 and $60 \mu\text{m}$. The simulation was run at distinct thicknesses of 5, 20, 40, 60, 80 and $100 \mu\text{m}$.

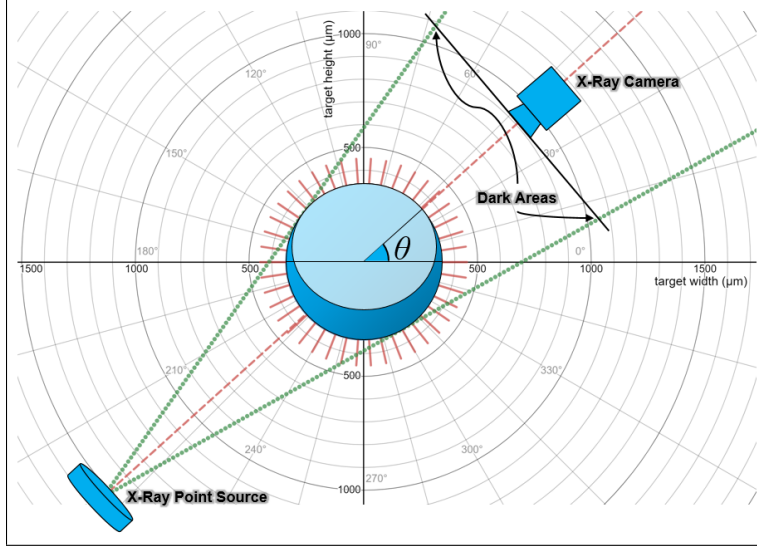


Figure 3.1: Cryogenic x-ray target characterization simulated by *SPARROW*. The dark blue meniscus in the target represents liquid DT fuel that has entered from the fill tube. The light blue region above indicates the bubble. The x-ray camera is represented as viewing from $\theta = 42^\circ$. The red lines (each 8.66° apart) show the angles that the simulation was run at for each of the distinct thicknesses.

However, the $5 \mu\text{m}$ run was outside the range of thicknesses over which Equations (1), (2) and (3) were developed. For each thickness, the simulation was run with the point source placed every 8.66° (see Figure 3.1) with θ going from -90° to 90° , with 0° being perpendicular to gravity and level with the target center.

3.2 Analysis of Simulated Data

The data collected from running *SPARROW* simulations are shown in Figure 3.2. c' is the semi-minor axis of the elliptical meniscus bubble; $r = 430 \mu\text{m}$ is the radius of the target. Thus, $\frac{c'}{r}$ represents the normalized semi-minor axis. $\frac{c'}{r}$ was calculated for an array of viewing angles and thicknesses. Figures 3.2a and 3.2b show different regressions of the same data. The vertical black line in both plots signifies the viewing angle, -23.97° , from which the x-ray camera will view the target on OMEGA.

The linear fit in Figure 3.2a provides a complete solution to the problem of how to predetermine the final layer thickness of an OMEGA fill tube target where θ will be -23.97° . Based on the $\frac{c'}{r}$ obtained from fitting an ellipse to a target x-ray image, the vertical black line will be interpolated along to calculate the final thickness.

The collected data revealed a sinusoidal relationship between viewing angle and the normalized semi-minor axis. Results also showed that the amplitude of the sinusoidal rela-

tionship correlates directly with thickness. The data was fitted to the form

$$\frac{c'}{r}(T, \theta) = [P(T)]\cos(A\theta) - BT + D \quad (4)$$

where T represents the final thickness of the frozen ice layer; θ represents the viewing angle; and A, B , and D represent constants to be fit. $P(T)$ represents a polynomial of thickness.

The Cryogenic Fill-tube Test Facility (CFTF) was previously built at LLE to test the possibility of using a fill tube. The CFTF includes x-ray and shadowgraphy cameras for characterization. Unlike the prototype shown in Figure 2.4, the x-ray camera on the CFTF views the target from the horizontal. Previous experiments conducted on the CFTF verified the linear relationship between semi-minor axis and thickness for $\theta = 0$ only. However, it is unknown what kind of association exists between $P(T)$ and thickness at other angles. To investigate this, the data was fit using both linear and quadratic polynomials to see if one fit better than the other.

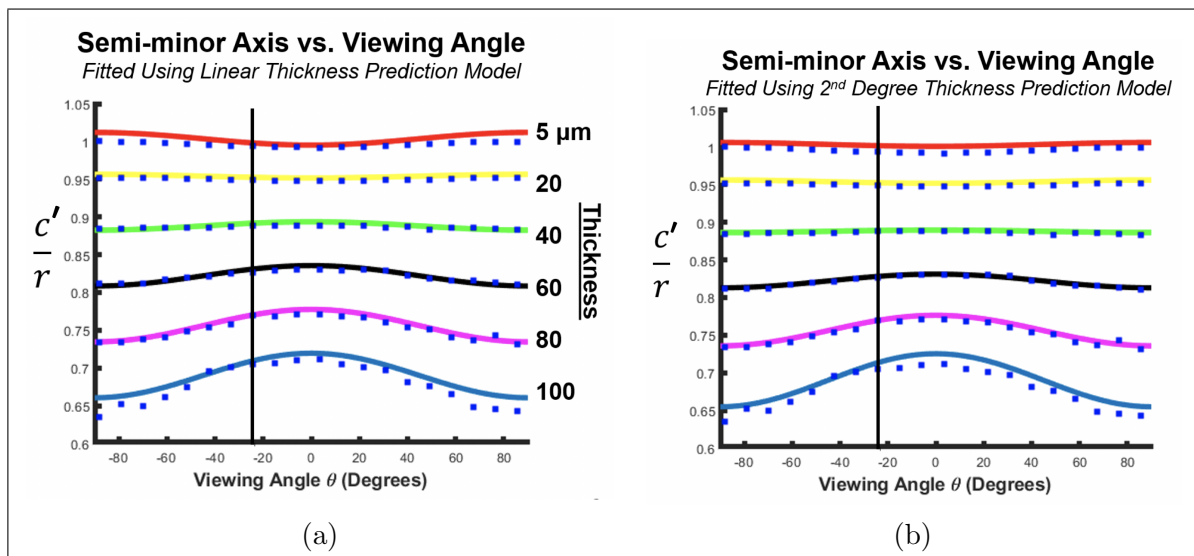


Figure 3.2: Simulated $\frac{c'}{r}$ as a function of θ for each of six distinct ice thicknesses. $\theta = 0$ represents viewing the target directly from horizontal. The simulated data were fit using both (a) first- and (b) second-degree polynomials.

Regression was used to fit Equation (4) using first- and then second-degree polynomials to determine which (linear or quadratic) fit better. The results depicted in Figure 3.2

produced the fits

$$\frac{c'}{r}(T, \theta) = [(3.99\text{e-}4)T - 1.04\text{e-}2] \cos(2\theta) - 0.0033T + 1.02 \quad (5)$$

$$\frac{c'}{r}(T, \theta) = [(4.66\text{e-}6)T^2 - (9.09\text{e-}5)T - (2.21\text{e-}3)] \cos(2\theta) - 0.0033T + 1.02 \quad (6)$$

where T is measured in μm . Both equations fit with a coefficient of determination of 0.997. Figure 3.2 shows that below a certain thickness threshold, the semi-minor axis of the bubble viewed switches from appearing largest when viewed horizontally to appearing largest when viewed from 90° to horizontal. Note how the sinusoidal relationship between viewing angle and normalized semi-minor axis inverts between $T = 20 \mu\text{m}$ and $T = 40 \mu\text{m}$.

To calculate the threshold, Equations (5) and (6) were solved for T such that the expression $P(T) = 0$. $P(T)$ is the bracketed expression that $\cos(2\theta)$ is scaled by. From Equation (5), the threshold is $T = 25.92 \mu\text{m}$ in the linear model. However, it is $T = 33.62 \mu\text{m}$ in the quadratic model in Equation (6). To determine where the actual inversion was, the simulation was rerun at closer thicknesses of 25.92, 29.77, and 33.62 μm . The results from this were then fit both linearly and quadratically with Equation (4). The linear fit produced an inflection point at 30.346 μm ; the quadratic fit produced 30.75 μm . The mean of these two was 30.55 μm . Therefore, 30.55 μm was assumed to be the inflection point.

To gain some insight into the threshold behavior, the simulation was run at $\theta = 90^\circ$ and $\theta = 0$ for thicknesses below, at, and above the threshold, shown in Figure 3.3. In the simulated x-ray images, the midpoint of the bubble does not fall on the midpoint of the target. However, the bubble transitions from having a horizontal major axis when viewed at $\theta = 0$ in (a) to having it vertically in (c). So, the bubble transitions from being wider than it is tall to taller than it is wide.

3.3 Model Testing

The linear and quadratic models each performed more accurately for different viewing angles and thicknesses. Below the threshold of $T = 30.55 \mu\text{m}$, the linear model made more accurate predictions within 45° of perpendicular to gravity. For angles greater than 45° , the quadratic

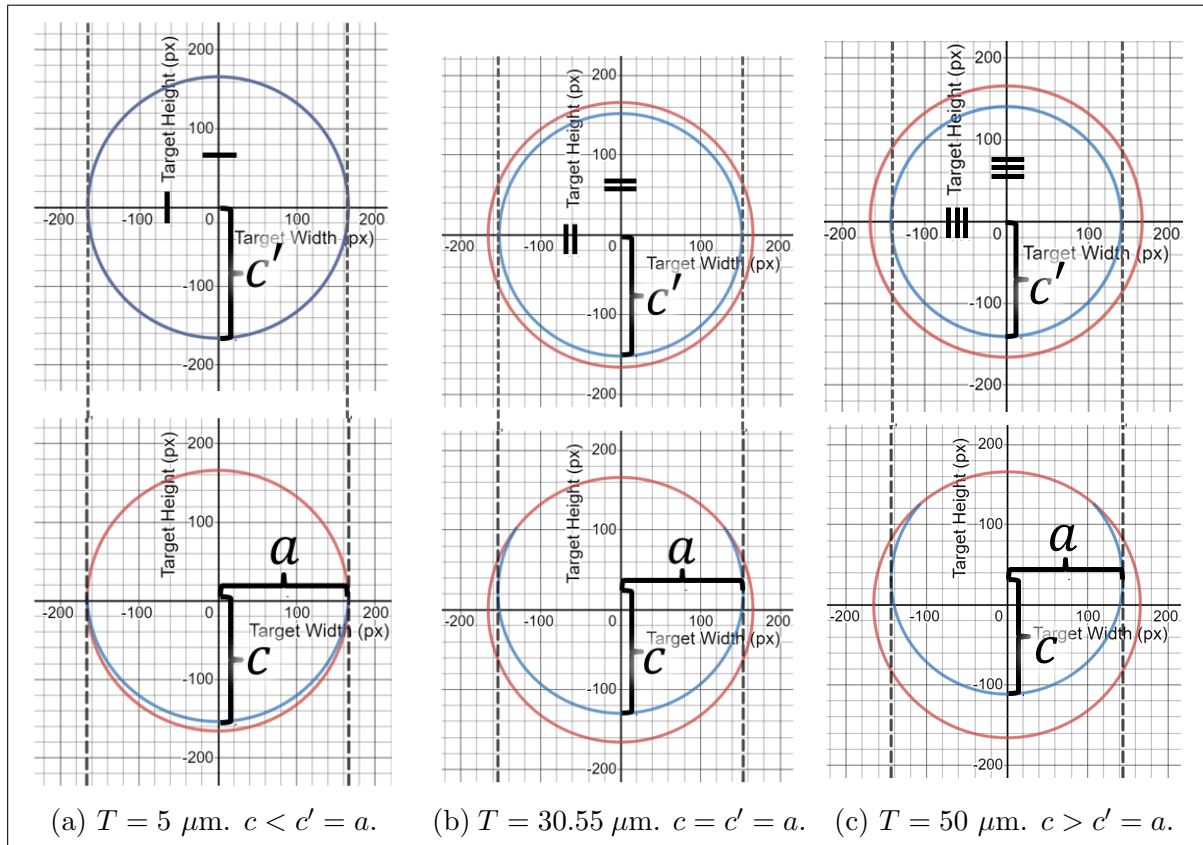


Figure 3.3: Simulated uncooled targets of final ice layer thicknesses (a) less than the modeled relationship inversion threshold, (b) at the threshold and (c) greater than the threshold. Targets are viewed from 90° above horizontal (top) and at horizontal (bottom). Below the threshold, the meniscus bubble (blue) is larger when viewed 90° above horizontal. Above the threshold, the meniscus bubble is larger when viewed directly at horizontal.

model made more accurate predictions. Above the threshold, the opposite was observed.

The thickness predetermination model was tested against 19 CFTF fills of cryogenic DT targets with $\theta = 0$. Experiments in which ice layers exhibited more than 10% of surface area being at least $16 \mu\text{m}$ outside the mean radius of the ice layer were considered poor quality targets. The testing dataset size was reduced to 14 after poor quality targets were excluded. For these 14, thickness predictions were compared against x-ray measurements for accuracy because shadowgraphy measurements exhibited more variability. X-ray images are also known to provide more accurate thickness measurements. The predicted thickness was on average within $2 \mu\text{m}$ of the measured average layer thickness, as shown in Figure 3.4. This satisfies the $2\text{-}\mu\text{m}$ accuracy requirement of LLE's experimental program.

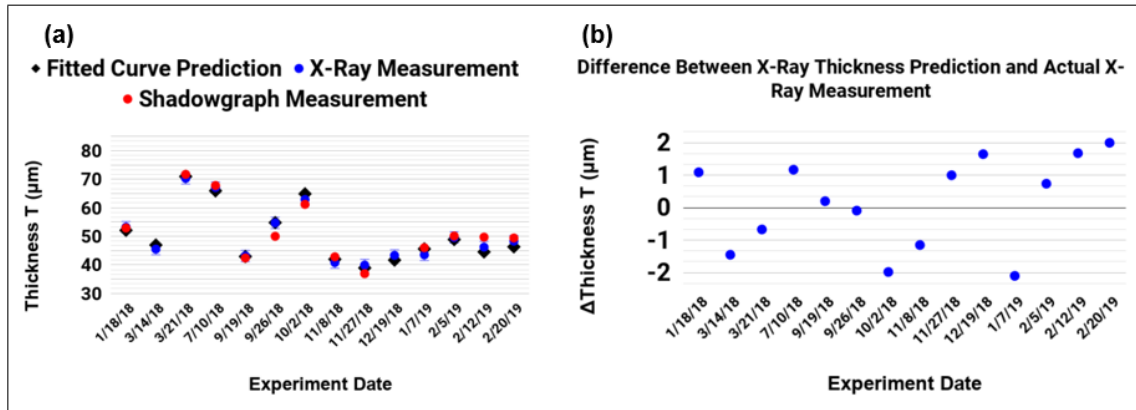


Figure 3.4: (a) Thickness prediction vs. measurements; (b) difference between prediction and x-ray measurement. The difference represents the distance between the black diamond and the blue circle for a given target.

Having satisfied the experimental program accuracy requirement, the developed thickness prediction formulas in Equations (5) and (6) will be implemented into the automated control loop of Ref. 7. Thus, cryogenic target filling can now be automated for OMEGA fill tube targets when viewed from 23.97° . It can also be automated for any other arbitrary angle.

4 Machine Learning Model

The second goal of this work was (1) to quantify the improvement that a new cryogenic filling mechanism can deliver to the neutron yield of a cryogenic DT implosion and (2) to use this measure to improve yield predictions.

4.1 Feature Selection

In order to quantify the yield increase that a new cryogenic filling mechanism can deliver, a group of features relating to cryogenic targets was selected from a dataset of implosion experiments conducted on the OMEGA laser within the past two years. Older shots were omitted to avoid externalities (e.g., new modules that would skew the data). These data were augmented with features that had been used to develop a previous model.⁸

The features collected from the dataset are listed in Table 1. The previously used features (those that are unrelated to target quality) are the last six entries. I_{RMS} represents the root mean square (RMS) nonuniformity of the ice layer of frozen targets. This estimate is calculated from the nonuniformity of the optical shadowgraphy bright ring. The same process is applied to the target shell ring to calculate S_{RMS} .

A_S , A_M , C_E , A_D , and C_D are measurements of the quality of the exterior polymer target that holds DT inside a target. Increases in all these values negatively impact implosion yield. Large C_E and C_D decrease implosion yield more than large A values because they indicate that target imperfections are skewed toward either the top or bottom. For LLE experiments, this skew is generally toward the top of the target. Elliptical and dendrite defects are two types of target imperfections that result from the current diffusion-filling process. Dendrite defects have a more negative impact on yield than elliptical defects.

Exploratory Data Analysis (EDA) of these features revealed that the initial horizontal offset of the crystal seed held no relationship with neutron yield nor implosion velocity. EDA also revealed (1) a negative correlation between between Y and T and (2) an unexpected positive correlation between Y and I_{RMS} . However, high-RMS ice layers are known to reduce implosion velocity and neutron yield.⁹ The data's positive correlation between B-band RMS and yield contradicts a physical property. Thus, this trend was assumed to reduce the accuracy of a model's predictions. This was investigated by plotting the density of I_{RMS} for relatively low as well as relatively high thicknesses T because layer thickness has been shown to significantly influence Y (see Figure 4.1). The density plot in Figure 4.1 shows that as T increases, I_{RMS} decreases. This is why Y exhibits a positive correlation with I_{RMS} when

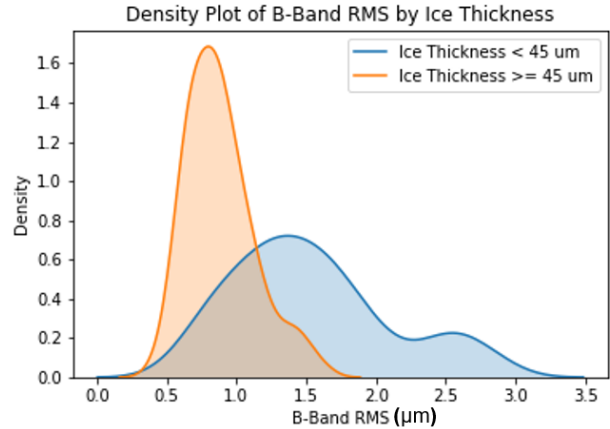


Figure 4.1: Density Plot of B-band RMS by Layer Thickness. At higher thicknesses, I_{RMS} is approximately normal and centered at $\sim 0.75 \mu\text{m}$. At lower thicknesses, I_{RMS} is bimodal and generally greater, with centers at $\sim 1.3 \mu\text{m}$ and $\sim 2.6 \mu\text{m}$.

<i>Inputs</i>	
Symbol	Name
I_{RMS}	Estimated thickness nonuniformity of solid DT layer (μm)
T	Final ice layer thickness (μm)
τ	Age of DT fuel (s)
d_X	Initial crystal seed horizontal offset (μm)
d_Y	Initial crystal seed vertical offset (μm)
S_{RMS}	RMS of target shell (μm)
A_S	Area of small-sized elliptical defects on target (μm^2)
A_M	Area of medium-sized elliptical defects on target (μm^2)
C_E	Centroid of elliptical defects on target (μm)
A_D	Area of dendrite defects on target (μm^2)
C_D	Centroid of dendrite defects on target (μm)
δ_{SSD}	Application of SSD (binary)
R_T	Range of ion temperature measurements (K)
V_{sim}	Simulated implosion velocity (m/s)
M_{sim}	Simulated target mass at stagnation (μg)
ρR_{sim}	Simulated areal density ($\text{kg}/\mu\text{m}^2$)
R_0	Outer radius of target (μm)
<i>Output</i>	
Symbol	Name
\hat{Y}_{exp}	Predicted neutron yield

Table 1: Symbols and descriptions of the initial feature space and output of the model developed to predict neutron yield.

considered independent of T . T impacts yield more than I_{RMS} . So, for low- I_{RMS} targets (large T), yield was lower than high- I_{RMS} targets not because of I_{RMS} itself, but because of T . To account for this in training the model, a second-order feature

$$Q_I = (I_{RMS})(T) \quad (7)$$

was added to the dataset to describe the quality of the solid layer more generally. Q_I accounts for both layer uniformity and thickness. This eliminated the incorrect trend that

was occurring between I_{RMS} and Y . Q_I correlates negatively with Y . Ultimately, the dimensionality of the model dataset was reduced by omitting the horizontal offset of the initial crystal seed, the bright ring RMS, and the layer thickness from training data; the latter two were replaced with layer quality Q_I .

4.2 Model Development

After dimensionality reduction, an investigation into the possibility of using a neural network to analyze the data was conducted on the entirety of the experimental dataset of cryogenic target shots at LLE within the past two years. This dataset contains 400 distinct features but only 215 data points. Each feature is either a simulated or observed measurement (e.g., those in Table 1). Each data point is a set of feature values corresponding to an imploded target (a “shot”). Having more features than data points suggested a neural network would have a low probability of successfully predicting neutron yields in this context. One of the more commonly used configurations for training neural networks was used. This was a 12-layer neural network with rectified linear unit (ReLU) activation. This was also configured with Sigmoid activation functions on deeper neurons. This performed with an accuracy of 0.12%, verifying that neural networks are currently not applicable for yield prediction in the context of cryogenic shots.

Subsequently, various predictive models were trained on the cryogenic target shot data using five-fold cross-validation, wherein 5 distinct 20% portions of the dataset were used as holdout testing data to be used for model evaluation after the model was trained on the other 80%. The metrics calculated from evaluating the different models on these 5 groups were the mean absolute error (MAE) and root mean square error (RMSE). For each model, these two metrics were averaged across the 5 runs and subsequently used for evaluation. Figure 4.2 shows a comparison of various models, ranked based on these metrics. The MAE and RMSE were compared against those of (a) a naive model that exclusively predicts the median yield and against (b) a developed model that does not factor in target data.⁸ Both (a) and (b), the control models, are shown in black in Figure 4.2. (a) is labeled “Median”; (b) is labeled “Omitting Target Data.”

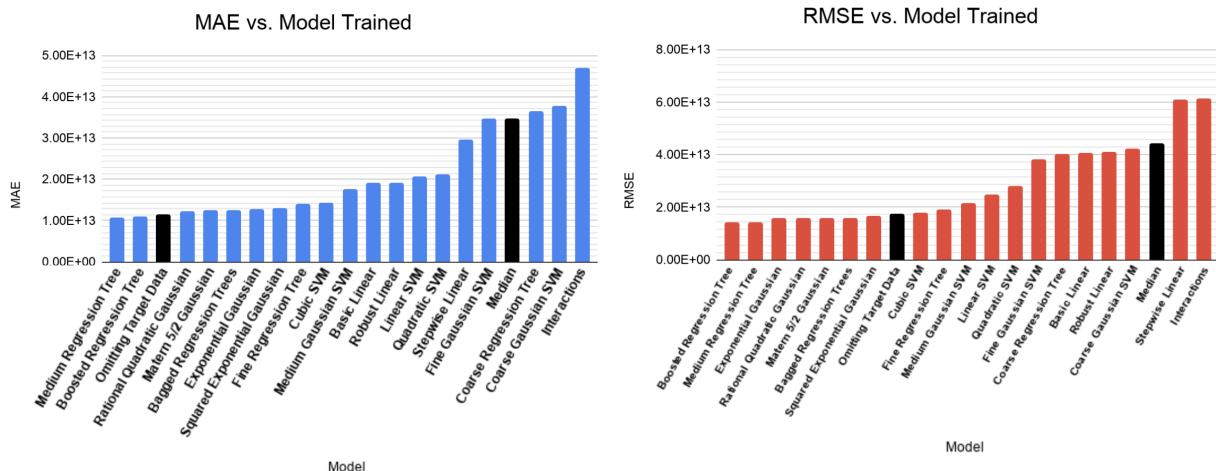


Figure 4.2: Mean absolute error (MAE) and root-mean-squared error (RMSE) compared across various yield prediction models.

4.3 Analysis of Model Output

Two models showed improvement when trained on data augmented with target parameters. The medium-grained regression tree showed the smallest MAE from experimental data. At 1.08×10^{13} neutrons, this demonstrated a 5.46% decrease from the model trained without target data (1.14×10^{13} neutrons). The ensemble of boosted trees showed the smallest RMSE. At 1.43×10^{13} neutrons, this demonstrated a 17.17% decrease from the model trained without target data ($1.73 \cdot 10^{13}$ neutrons). Having lower error values demonstrates that these two models performed better than the others.¹⁰

The best performing models were decision trees, which generally “overfit” data (fit noise in the data rather than physical trends).¹¹ Models that overfit data are observed to perform better on training data at the cost of performance on testing data; this performance can be compared using MAE and RMSE. Overfitted models tend to mistake noise in data for physical relationships. As shown in Figure 4.3, the two best performing models had lower MAE and RMSE values on their training data. With the ensemble model, RMSE increased 142% between training and testing data; MAE increased 138%. The medium regression tree RMSE increased 21% between training and testing data; MAE increased 25%. These results indicate that the ensemble model overfit the data significantly more than the medium regression tree. This overfitting was mitigated through cross-validation but still present. By

separating the dataset into 5 groups of data, each model is iteratively trained on the first four randomly selected samples (“folds”) of data. Then, the final fold is used to test the accuracy of the model. Because the model is trained on all four folds iteratively, it is less likely to overfit noise in a single fold. This thus mitigates overfitting.

Neutron yields for experiments conducted on OMEGA are generally on the order of 10^{13} or 10^{14} neutrons. Because the RMSE of the models were also on the order of 10^{13} , none of these machine learning models are suitable for real-time high-precision predictions; however, they quantify the impact of target quality on neutron yield.

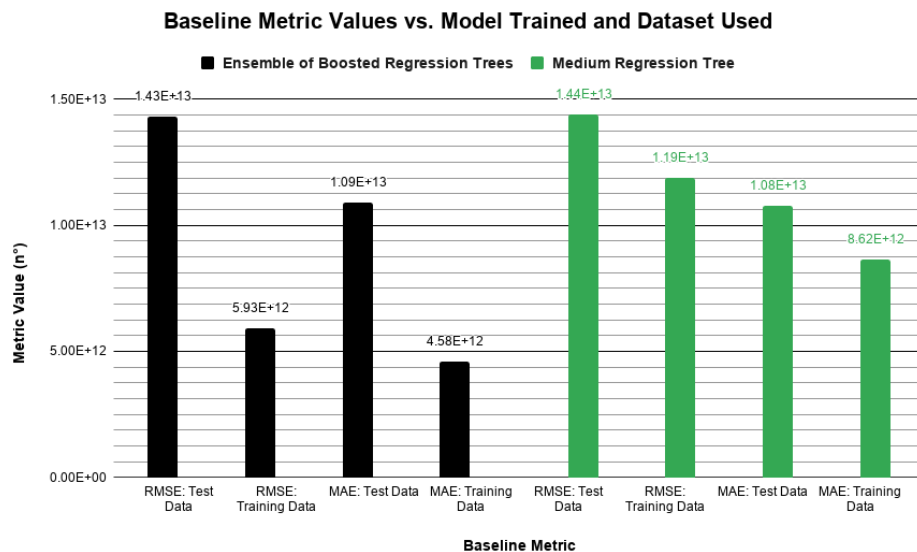


Figure 4.3: Comparison of the RMSE and MAE values of the boosted ensemble and medium regression decision tree machine learning models on testing and training datasets.

The decision tree models in Figure 4.3 were computed by the following process for each of the five folds of the cross-validation.¹² Twelve different numeric yield outcomes (evenly spaced based on the distribution of yields) were algorithmically established. An array of rules were then automatically fit to the training data (e.g., if δ_{SSD} is disabled, then Y will not exceed 1.2×10^{14} neutrons). For testing, a distinct tree would, given a data point with the input parameters in Table 1, assign a certainty (percent confidence) to each outcome. The final prediction for the data point was the weighted average of these outcomes.

Decision trees are inherently different from other models tested such as linear regression

(where the relationship between the prediction \hat{Y}_{exp} is assumed to be linear with the input variables) and gaussian regression (where all input variables are assumed to be normally distributed).¹³ The other models are less optimal for highly complex datasets but they generally do not overfit to the extent that decision trees do.

This verified that the neutron yield of implosions is multivariate and nonlinear. This also showed that cryogenic target quality highly correlates with neutron yield. Finally, the increased accuracy of the model resulting from training with target data shows the material importance of target quality in the goal of achieving nuclear ignition and burn.

5 Conclusion

In this work, two models were created. The first, a ray-tracing model *SPARROW*, is for use in filling cryogenic targets on the new fill-tube system on the OMEGA laser. The second leverages machine learning to predict neutron yield and quantify the significance of target quality on that yield.

SPARROW was developed to predetermine the final solid layer thickness of cryogenic targets filled using the fill-tube fixture. This was previously not possible for targets viewed from any angle. *SPARROW* was created using relationships previously learned from x-ray images of liquid fills viewed in the horizontal plane. Results from this model were fit to linear and quadratic polynomials. These give analytic expressions that allow the thickness to be determined for any viewing angle. For the angle at which the fill tube will be fielded on OMEGA, the linear model is optimal. The model will be implemented to fill cryogenic targets automatically to a desired thickness. Preexisting target fills imaged perpendicular to gravity were used as testing data. The model performed within the 2 μm accuracy specification of LLE's experimental program on these data.

The machine learning model was created to quantify the significance of target quality to fusion yield. Cryogenic shot data from OMEGA was first compiled for training. Then, nineteen types of predictive models were trained and compared for performance. The ensemble of boosted trees model was the most accurate. Testing of this model showed that target

quality data improved neutron yield predictions by 17%. This indicates that target quality improvements using the cryogenic fill-tube fixture have a material impact on experimental yields.

When the cryogenic fill-tube is fielded on OMEGA and used for implosions, data from the fill-tube fixture can be used in the yield prediction machine learning model. Data such as the range in temperature from the start to the end of the filling process, and the length of time required for filling could be included. Including these might provide insight into physical properties and further improve yield prediction accuracy.

6 Acknowledgements

I am thankful to Mr. Mark Wittman, Mr. Dean Bredesen, Dr. R. Stephen Craxton, Carwyn Collinsworth, and the 2019 high school students at LLE. Mr. Wittman and Mr. Bredesen provided mentorship. Dr. Craxton has managed the high school program since 1998, enabling over 260 students to participate in fusion research; he also provided advice for this work. Carwyn Collinsworth, a 2018 high school student, contributed to the foundation for this project. The thirteen other summer high school students of 2019 provided feedback.

References

- [1] R. S. Craxton, K. S. Anderson, T. R. Boehly, V. N. Goncharov, D. R. Harding, J. P. Knauer, R. L. McCrory, P. W. McKenty, D. D. Meyerhofer, J. F. Myatt, A. J. Schmitt, J. D. Sethian, R. W. Short, S. Skupsky, W. Theobald, W. L. Kruer, K. Tanaka, R. Betti, T. J. B. Collins, J. A. Delettrez, S. X. Hu, J. A. Marozas, A. V. Maximov, D. T. Michel, P. B. Radha, S. P. Regan, T. C. Sangster, W. Seka, A. A. Solodov, J. M. Soures, C. Stoeckl, and J. D. Zuegel, “Direct-drive inertial confinement fusion: A review,” *Physics of Plasmas*, vol. 22, no. 11, p. 110501, 2015.
- [2] D. R. Harding, J. Ulreich, M. D. Wittman, R. Chapman, C. Taylor, R. Taylor, N. P. Redden, J. C. Lambropoulos, R. Q. Gram, M. J. Bonino, and D. W. Turner, “Requirements and Capabilities for Fielding Cryogenic DT-Containing Fill-Tube Targets for Direct-Drive Experiments on OMEGA,” *Fusion Science and Technology*, vol. 73, no. 3, pp. 324–334, 2018.
- [3] T. C. Sangster, R. Betti, R. S. Craxton, J. A. Delettrez, D. H. Edgell, L. M. Elasky, V. Y. Glebov, V. N. Goncharov, D. R. Harding, D. Jacobs-Perkins, R. Janezic, R. L. Keck, J. P. Knauer, S. J. Loucks, L. D. Lund, F. J. Marshall, R. L. McCrory, P. W. McKenty, D. D. Meyerhofer, P. B. Radha, S. P. Regan, W. Seka, W. T. Shmayda, S. Skupsky, V. A. Smalyuk, J. M. Soures, C. Stoeckl, B. Yaakobi, J. A. Frenje, C. K. Li, R. D. Petrasso, F. H. Séguin, J. D. Moody, J. A. Atherton, B. D. MacGowan, J. D. Kilkenny, T. P. Bernat, and D. S. Montgomery, “Cryogenic DT and D2 targets for inertial confinement fusion,” *Physics of Plasmas*, vol. 14, no. 5, p. 58101, 2007.
- [4] A. J. Martin, R. J. Simms, and R. B. Jacobs, “Beta energy driven uniform deuterium–tritium ice layer in reactor-size cryogenic inertial fusion targets,” *Journal of Vacuum Science & Technology A: Vacuum, Surfaces, and Films*, vol. 6, pp. 1885–1888, 5 1988.
- [5] D. R. Harding, D. Whitaker, and C. Fella, “Growth of a solid D-T crystal from the liquid inside inertial confinement fusion targets,” in *Fusion Science and Technology*, vol. 70, pp. 173–183, American Nuclear Society, 8 2016.

- [6] D. H. Edgell, R. S. Craxton, L. M. Elasky, D. R. Harding, L. S. Iwan, R. L. Keck, L. D. Lund, S. J. Verbridge, M. D. Wittman, A. Warrick, T. Brown, and W. Seka, “Three-dimensional characterization of cryogenic target ice layers using multiple shadowgraph views,” in *Fusion Science and Technology*, vol. 49, p. 624, American Nuclear Society, 2006.
- [7] C. R. Collinsworth, “Real Time X-Ray Analysis of Liquid-DT Fill Level in Fill-Tube Capsules to Control Solid-Layer Thickness,” **Project Report**, Laboratory for Laser Energetics Summer High School Research Program, 2018.
- [8] V. Gopalaswamy, R. Betti, J. P. Knauer, N. Luciani, D. Patel, K. M. Woo, A. Bose, I. V. Igumenshchev, E. M. Campbell, and K. S. Anderson, “Tripled yield in direct-drive laser fusion through statistical modelling,” *Nature*, vol. 565, no. 7741, p. 581, 2019.
- [9] R. L. McCrory, S. P. Regan, S. J. Loucks, D. D. Meyerhofer, S. Skupsky, R. Betti, T. R. Boehly, R. S. Craxton, T. J. B. Collins, J. A. Delettrez, D. Edgell, R. Epstein, K. A. Fletcher, and others, “Direct-drive inertial confinement fusion research at the Laboratory for Laser Energetics: charting the path to thermonuclear ignition,” *Nuclear Fusion*, vol. 45, pp. S283–S290, 10 2005.
- [10] D. H. Wolpert and W. G. Macready, “No free lunch theorems for optimization,” *IEEE Transactions on Evolutionary Computation*, vol. 1, pp. 67–82, 4 1997.
- [11] L. Breiman, “Statistical Modeling: The Two Cultures (with comments and a rejoinder by the author),” *Statist. Sci.*, vol. 16, no. 3, pp. 199–231, 2001.
- [12] J. R. Quinlan, “Generating production rules from decision trees,” (Cambridge, MA), pp. 304–307, 1987.
- [13] J. Quiñero and C. E. Rasmussen, “A Unifying View of Sparse Approximate Gaussian Process Regression,” *Journal of Machine Learning Research*, vol. 6, pp. 1939–1959, 2005.